Dorsal/NF-κB exhibits a dorsal-to-ventral mobility gradient in the Drosophila embryo

Hadel Al Asafen[a,1], Natalie M. Clark[b,1], Etika Goyal[a,1], Sadia Siddika Dima[a], Hung-Yuan Chen[a], Thomas Jacobsen[c], Rosangela Sozzani[b], and Gregory T. Reeves[a,d,*]

[a] Artie McFerrin Department of Chemical Engineering, Texas A&M University, College Station, TX 77843

[b] Department of Plant and Microbial Biology, North Carolina State University, Raleigh, NC 27606

[c] Department of Chemical and Biomolecular Engineering, North Carolina State University, Raleigh, NC 27606

[d] Interdisciplinary Graduate Program in Genetics and Genomics, Texas A&M University, College Station, TX 77843

[1] These authors contributed equally to this work

[*] To whom correspondence should be addressed:
100 Spence Street
Texas A&M University, Chemical Engineering Dept
College Station, Texas 77843 MS 3122
979-862-4021
gtreeves@tamu.edu

Abstract

Morphogen-mediated patterning is a highly dynamic developmental process. To obtain an accurate understanding of morphogen gradient formation and downstream gene expression, biophysical parameters such as protein mobilities must be quantified *in vivo*. The dorsal-ventral (DV) patterning of early *Drosophila* embryos by the NF-κB homolog Dorsal (Dl) is an excellent system for understanding morphogen gradient formation. Dl gradient formation is controlled by the inhibitor Cactus/IκB (Cact), which regulates the nuclear import and diffusion of Dl protein. However, quantitative measurements of Dl mobility and binding are currently lacking. Here, we use scanning fluorescence correlation spectroscopy to quantify the mobility of GFP-tagged Dl. We find that the DNA binding of Dl-GFP, which affects its mobility, varies along the DV axis, with highest DNA binding on the ventral side. Moreover, we also observe that the time scale for Dl-GFP to exit the nucleus is longer in the ventral and lateral regions of the embryo, which is consistent with stronger DNA binding. Using analysis of mutant alleles of *dl* tagged with GFP, we conclude that Dl-GFP/Cact interactions in the nuclei are responsible for the variation in Dl-GFP/DNA binding along the DV axis, which impacts our understanding of the spatial range of the Dl gradient and the robustness and precision of downstream gene expression. Thus, our results highlight the complexity of morphogen gradient dynamics and the ability of quantitative measurements of biophysical interactions to drive biological discovery.

Introduction

Tissues in a developing organism are patterned by short and long-range signaling achieved through morphogen concentration gradients, which carry the positional information necessary to control gene expression in a spatially dependent fashion. In the past two decades, studies using GFP-tagged morphogens -- including early *Drosophila* morphogens Bicoid and Dorsal; Dpp in the wing imaginal disc; and the Hedgehog, Wnt, and TGF-β families in vertebrates -- have revealed that the establishment of morphogen gradients is a highly dynamic and complex process (Delotto et al., 2007; Entchev et al., 2000; Gregor et al., 2007; Holzer et al., 2012; Luz et al., 2014; Reeves et al., 2012; Ribes et al., 2010; Teleman & Cohen, 2000; Wallkamm et al., 2014; Wartlick et al., 2011; Williams et al., 2004; Zhou et al., 2012). To move toward a quantitative understanding of morphogen signaling and downstream gene expression patterns, several key biophysical parameters related to gradient formation, including diffusivity and binding, must be measured.

Dorsal (Dl), one of three *Drosophila* orthologs to mammalian NF-κB (Steward, 1987), acts as a morphogen to pattern the dorsal-ventral (DV) axis of blastoderm stage (1-3 h old) *Drosophila*

embryos. Dl is initially distributed uniformly along the DV axis (Roth et al., 1989; Steward et al., 1988). After the 9th nuclear division cycle, when the nuclei migrate to the periphery of the syncytial embryo, Dl begins to accumulate in ventral nuclei, and is excluded from dorsal nuclei (Roth et al., 1989; Steward et al., 1988). This DV gradient in Dl nuclear concentration is due to signaling through the Toll receptor on the ventral side of the embryo (Anderson, Bokla, et al., 1985; Anderson, Jürgens, et al., 1985; Belvin & Anderson, 1996). In the absence of Toll signaling, Dl remains bound by the cytoplasmic tethering protein Cactus (Cact), the *Drosophila* IκB homolog (Geisler et al., 1992; Kidd, 1992), and thus localized to the cytoplasm (Belvin et al., 1995; Bergmann et al., 1996; Reach et al., 1996; Whalen & Steward, 1993). On the ventral side, Toll signaling acts through Pelle kinase to phosphorylate Cact, which causes dissociation of the Dl/Cact complex and degradation of Cact (Daigneault et al., 2013). Once freed from binding to Cact, Dl enters the nucleus and regulates the expression of more than 50 target genes, which initiate further signaling pathways and specification of the embryo's germ layers (Chopra & Levine, 2009; Moussian & Roth, 2005; Reeves & Stathopoulos, 2009; Schloop, Bandodkar, et al., 2020; Stathopoulos & Levine, 2002, 2004). Toll signaling also phosphorylates Dl, which has been shown to increase Dl nuclear localization (Drier et al., 1999, 2000; Gillespie & Wasserman, 1994; Whalen & Steward, 1993).

While this well-established mechanism rapidly initiates Dl gradient formation, recent work has revealed complex dynamics in the further maturation of the gradient. In particular, live imaging of fluorescently-tagged Dl proteins has shown that the Dl nuclear gradient grows slowly during interphase and collapses during mitosis (Delotto et al., 2007; Reeves et al., 2012). Quantification of the gradient levels has shown that over the course of nuclear cycle 10-14, Dl (both nuclear and cytoplasmic) accumulates on the ventral side of the embryo, causing the peak of the Dl gradient, in the ventral-most cells, to grow steadily over time (Carrell et al., 2017; Liberman et al., 2009; O'Connell & Reeves, 2015; Reeves et al., 2012; Schloop, Carrell-Noel, et al., 2020). In particular, diffusion and nuclear capture of Dl, both of which are regulated by Cact, are proposed to control the continuous growth of the Dl gradient peak (Carrell et al., 2017). Nonetheless, the diffusivity and nuclear transport rates are not quantitatively known. Furthermore, our previous work has suggested that Dl/Cact complex also is present in the nucleus, which has implications for the apparent spatial range of the Dl gradient, as well as for the robustness and precision of gene expression (Al Asafen et al., 2020; O'Connell & Reeves, 2015). Therefore, to fully understand the dynamics of Dl gradient formation and gene regulation, measurements of the biophysical parameters governing Dl mobility (specifically diffusivity, nuclear transport, and binding to DNA) are needed.

Here we employ scanning fluorescence correlation spectroscopy (scanning FCS) techniques to measure the mobility of Dl in live embryos. Scanning FCS techniques involve rapid and repeated acquisition of fluorescent imaging data using confocal microscopy. First, we apply a specific scanning FCS method known as Raster Image Correlation Spectroscopy (RICS) to autocorrelate

106 GFP-tagged Dl over space and time in a small region of the embryo (Digman, Brown, et al., 2005;
107 Digman, Sengupta, et al., 2005). The shape of this autocorrelation function is then analyzed to
108 infer protein diffusion, which reveals two pools of Dl-GFP, mobile and immobile. Notably, we
109 observed that the fraction of immobile Dl varies along the DV axis. Cross-correlation RICS
110 (ccRICS), which uses two different fluorophores (GFP and RFP, in this case), suggests that the
111 DV variation in immobile fraction is the result of a higher fraction of Dl binding to the DNA on
112 the ventral side than on the dorsal side. In addition, we employ Pair Correlation Function (pCF)
113 technique to compute the correlation between two pixels along a line scan, allowing us to visualize
114 barriers to Dl movement (Digman & Gratton, 2009; Hinde et al., 2010). We show that the tendency
115 of a Dl-GFP molecule to exit the nucleus also displays variation along the DV axis. When
116 examining mutants that mimic the Dl gradient at different DV positions, the RICS and pCF data
117 corroborate these findings. We propose two competing hypotheses to explain the DV variation in
118 Dl/DNA interactions: that Toll phosphorylation of Dl may increase Dl/DNA interactions on the
119 ventral side, or that Cact may bind Dl in the nuclei, which would prevent Dl from binding DNA
120 in dorsal regions of the embryo. We test these competing hypotheses using mutant alleles of *dl* and
121 conclude that Dl/Cact binding in dorsal nuclei prevents DNA binding, suggesting that further
122 imaging of Cact may be needed to fully understand Dl-dependent gene expression. This result
123 reveals a Dl gradient that has greater dynamic range, spatial range, robustness, and precision than
124 previously understood (Al Asafen et al., 2020; Liberman et al., 2009; O'Connell & Reeves, 2015;
125 Reeves et al., 2012; Schloop et al., 2025).
126
127 **Results**
128
129 **Quantification of Dl Mobility Reveals a Dorsal-to-Ventral (DV) Gradient**
130 To measure the mobility of Dl in the embryo, we performed Raster Image Correlation
131 Spectroscopy (RICS) analysis on embryos carrying a monomeric GFP-tagged Dl (Carrell et al.,
132 2017) and an H2Av-RFP construct in a *dl* heterozygous background (hereafter referred to as Dl-
133 GFP embryos; see Materials and Methods). We performed RICS analysis in different locations
134 along the DV axis (Fig. 1A) of nuclear cycle 12-14 embryos, when the Dl gradient is clearly
135 defined and detectable. Specifically, we rapidly imaged small (pixel size $\leq$ 0.1 μm, 256x256
136 pixels; see Methods) regions of the embryo (Fig. 1B, Fig. S1A-D and Movies S1-3) and calculated
137 2D autocorrelation functions (ACFs; Fig. 1B and Equation 1 in Materials and Methods). The ACFs
138 each have a fast (ξ) and slow (η) direction due to the rapid movement and line retracing of the
139 confocal scan, respectively (Fig. 1C,D). We then fit a one-component, pure diffusion model to
140 these ACFs (Fig. 1C and Equation 2 in Materials and Methods; see also Supplemental
141 Information), which allowed us to estimate apparent diffusivities. We found that the apparent Dl
142 diffusivity varied with the nuclear-to-cytoplasmic ratio (NCR) of Dl-GFP intensity, which we take
143 as a proxy for position along the DV axis of the imaged region because embryos were mounted in
144 random DV orientations (Fig. 1A). In particular, the apparent diffusivity was lower on the ventral
145 side of the embryo than on the dorsal side (Fig. 1E). To test whether this trend is statistically

146 significant, we used linear regression, and found the slope of the apparent diffusivity from ventral-
147 to-dorsal to be statistically different from zero (p-value < 10^{-4}; Fig. 1E).
148
149 Considering that, on the ventral side of the embryo, Dl is predominantly located in the nucleus,
150 whereas on the dorsal side, Dl is predominantly cytoplasmic, it is possible that the spatial variation
151 in the diffusivity arises from differences in the behavior of nuclear and cytoplasmic Dl. Therefore,
152 we segmented the nuclei and calculated the ACF for the nuclei and the cytoplasm separately (see
153 Supplemental Information). We found a ventral-to-dorsal trend in the apparent diffusivity of
154 nuclear-localized Dl-GFP, as estimated by fitting to the pure diffusion model (p-value < 10^{-4}, Fig.
155 1F). However, the apparent cytoplasmic diffusivities showed no statistically significant trend in
156 spatial variation (p-value 0.6; Fig. 1G). These results suggest that the observed gradient in Dl
157 mobility is specific to nuclear-localized Dl.
158
159 We reasoned that the gradient in the mobility of nuclear-localized Dl could be dependent on Toll
160 signaling, which not only favors the dissociation of the Dl/Cact complex, but also phosphorylates
161 Dl and increases its affinity for the nucleus (Drier et al., 1999, 2000; Gillespie & Wasserman,
162 1994; Whalen & Steward, 1993). To this end, we performed RICS analysis on three mutant lines
163 with "ventral-like" (*Toll*^{10B}; Schneider et al., 1991), "lateral-like" (*Toll*^{r4}; Schneider et al., 1991),
164 or "dorsal-like" (*pll*$^{2/7}$; Anderson and Nüsslein-Volhard, 1984) levels of nuclear Dl-GFP (Fig. S1E-
165 G). If the spatial gradient in Dl movement depends on Toll signaling, then we would expect *Toll*^{10B}
166 embryos to have the lowest apparent diffusivity, while *Toll*^{r4} and *pll*$^{2/7}$ embryos would have higher
167 apparent diffusivities. Accordingly, we found the apparent diffusivity of total (nuclear +
168 cytoplasmic) Dl-GFP is correlated to the strength of Toll signaling across the mutants (Fig. 1H).
169 Additionally, linear regression revealed a ventral-to-dorsal trend (p-value 10^{-3}; Fig. 1H; left side).
170 Similarly, the apparent diffusivity of nuclear Dl-GFP varies across these Toll signaling mutants
171 with a statistically significant trend (p-value 10^{-3}; Fig. 1H, center). In contrast, we did not see a
172 variation in apparent cytoplasmic Dl-GFP diffusivity in the mutants (p-value 0.14; Fig. 1H, right
173 side). It should be noted that these uniform Toll signaling mutants lack a shuttling mechanism that
174 concentrates Dl on the ventral side of wildtype embryos (Carrell et al., 2017), and as such, the
175 NCR observed in these mutants cannot be used as a direct positional variable for comparing
176 mutants to wild type. For this reason, we presented the mutant results as boxplots to highlight
177 overall trends rather than position-matched values. These results suggest that the variation of
178 mobility along the DV axis is downstream of Toll signaling.
179
180 **The Gradient of Apparent Diffusivity is Due to Immobilized Dl in the Nucleus**
181 Given that Dl is a transcription factor, it is likely that there are at least two pools of Dl: a freely
182 diffusing pool, and a DNA-bound (immobile) pool. As such, it is possible that the diffusivity is
183 constant, and the observed trend in apparent diffusivity, as inferred by the pure diffusion model,
184 would in fact be a trend in the immobile fraction of Dl. For example, if a significant pool of
185 immobile Dl exists, it would lower the apparent diffusivity, as estimated by a pure diffusion model.

186 To investigate this possibility, we fit a two-component diffusion model (Equation 3 in Materials
187 and Methods) to the ACFs described above. In the two-component model, Dl could be in two
188 states: freely diffusible and immobilized (Fig. 2A; see Supplemental Information for more details).
189 Thus, an additional adjustable parameter is required: the fraction of immobilized Dl, ϕ. To avoid
190 over-fitting, when using the two-component model, we fixed the diffusivity to be 3 $\mu m^2/s$,
191 consistent with the cytoplasmic diffusivity measured above (Fig. 1F, left side). In general, we
192 found the two-component model fit the ACFs better than the one-component model (Fig. 2B).
193 Furthermore, we found that ϕ_{nuc}, the fraction of immobilized Dl in the nuclei, varies along the
194 DV axis, with a statistically significant linear trend in NCR (p-value < 10^{-4}; Fig. 2C). In contrast,
195 in the cytoplasm, roughly 10-20% of Dl was immobilized (ϕ_{cyt}) in wildtype embryos, and the
196 variation in this fraction along the DV axis lacked a statistically significant trend (p-value 0.08;
197 Fig. 2D).
198
199 In the previously described Toll signaling mutants, the immobile fraction of nuclear Dl-GFP was
200 statistically highly correlated with Toll signaling strength (p-value < $10^{-4;}$ Fig. 2E, left side).
201 The immobile fraction in the cytoplasm in the Toll signaling mutants did not rise to a statistically
202 significant trend (p-value 0.06; Fig. 2E, left side).
203
204 Taken together, our RICS data from both wildtype and mutant embryos are indicative of a two-
205 component system where a pool of Dl is immobilized, and that the immobile pool, specifically in
206 the nuclei, is highly correlated to Toll signaling. If the immobile pool represents Dl/DNA binding,
207 then the expectation for a transcription factor interacting with DNA is that the concentration of
208 immobile Dl should be a saturating, increasing function of total nuclear Dl concentration. In
209 contrast, in such a saturating system, the *fraction* of immobile Dl, ϕ, is expected to decrease (or,
210 at best, remain constant) with increasing nuclear total Dl concentration. However, we are
211 observing the opposite trend (ϕ being positively correlated with nuclear Dl), suggesting that the
212 variation in the immobile Dl pool along the DV axis is dictated by more than simply the nuclear
213 Dl concentration.
214
215 **Dorsal/DNA binding exhibits a spatial gradient**
216 Our RICS results suggest that the spatial variation in nuclear Dl movement is due to a population
217 of immobilized Dl-GFP on the ventral side of the embryo. To test whether the immobilized Dl in
218 the nuclei is due to DNA binding, and whether there is a spatial gradient in DNA binding, we used
219 cross-correlation RICS (ccRICS; Digman et al., 2009) to measure the extent to which Dl (Dl-GFP)
220 and Histone (H2Av-RFP) may be bound to the same physical structure (in this case, DNA). The
221 ratio of the cross-correlation function (CCF) amplitude (Fig. 3A,B) to the ACF amplitude in the
222 red channel (H2Av-RFP channel; Fig. 3C) is proportional to the fraction of Dl bound to DNA, ψ
223 (see Supplemental Information)(Rippe, 2000; Weidemann et al., 2002). Note that it is possible for
224 the CCF amplitude to be negative (Dl-GFP avoidance of H2Av-RFP), in which case, the fraction
225 ψ could be viewed as zero. We found ψ has a statistically significant linear trend with NCR (p-

226 value < 10^{-4}; Fig. 3D). In some cases with high ψ, the overlap between Dl-GFP and H2Av-RFP
227 can be seen visually (Fig. S2A and Movie S4). Furthermore, in dorsal regions, the correlation
228 between histone and Dl is indistinguishable from zero. In these cases, the low correlation can be
229 seen as the lack of peak in the CCF (Figs. 3B, S3B,C).
230
231 In the Toll signaling mutant embryos, ψ is also correlated with the levels of Toll signaling with a
232 statistically significant trend (p-value < 10^{-4}; Fig. 3E). Furthermore, ψ is indistinguishable from
233 zero in *pll*$^{2/7}$ mutants. Note that, as with the Dl diffusivity, there may not be a direct comparison
234 between ψ in the uniform Toll signaling mutants and the corresponding locations in wildtype
235 embryos.
236
237 To test whether ccRICS is an appropriate assay to detect Dl/DNA binding, we made a GFP-fused
238 allele of *dl* in which arginine 63 has been replaced by a cysteine (*dl*^{R063C}-*gfp*), which is in the highly
239 conserved DNA binding portion of the Rel homology domain and has been shown to severely
240 reduce Dl-mediated gene expression (Govind et al., 1996; Isoda et al., 1992). As this allele is
241 antimorphic (Isoda et al., 1992), we used a *nos*-Gal4 line to drive the expression of UAS-*dl*^{R063C}-
242 *gfp* (Brand & Perrimon, 1993) and overexpressed it in a maternal background of one copy of
243 transgenic *dl-mGFP* and zero copies of endogenous *dl* (see Materials and Methods). To directly
244 compare to a wildtype control, we also created a Gal4/UAS-driven wildtype allele of *dl* fused to
245 *gfp* (UAS-*dl*^{wt}-*gfp*). As predicted, the UAS-*dl*^{R063C}-*gfp* allele had a statistically lower value of ψ
246 on the ventral side than the wildtype control (p-value 10^{-3}; Fig. 3F, left side). In contrast, both
247 alleles had a low value of ψ on the dorsal side (p-value 0.3; Fig. 3F, right side). These results are
248 consistent with ψ being a measure of Dl/DNA binding.
249
250 Overall, the findings that both the DNA-bound pool and the immobilized pool of nuclear Dl-GFP
251 are correlated to both Toll signaling and the NCR suggest that DNA binding of Dl may be
252 responsible for its overall lowered mobility on the ventral side of the embryo. Furthermore, as
253 mentioned in the previous section, the trends of immobile fraction, ϕ, and fraction of Dl/DNA
254 interactions, ψ, both being positively correlated with nuclear Dl concentration is the opposite of
255 what would be expected for a saturating system consisting only of transcription factor/DNA
256 interactions.
257
258 **Dl Exhibits DV Variation in Nuclear Export Propensity**
259 Our RICS analysis revealed that Dl movement is lowest on the ventral side, where it is primarily
260 nuclear localized and a significant fraction is immobile, and highest on the dorsal side, where it is
261 primarily cytoplasmic. Thus, we reasoned that the ability of Dl to exit the nucleus could also vary
262 spatially. To determine whether there is spatial variation in Dl movement into or out of the nucleus,
263 we used Pair Correlation Function (pCF) analysis to measure any restriction of movement of Dl-
264 GFP across the nuclear envelope (Digman & Gratton, 2009, 2011; Hinde et al., 2010). Here it is
265 important to state the term "movement" can be ambiguous, and in other sections, movement refers

266 to apparent diffusion, which is random, passive motion inside the nucleus or cytoplasm In this
267 section, movement refers to the propensity of Dl to exit the nucleus.
268
269 In contrast to RICS, which uses 2D raster scans of the embryo, pCF requires line scans. For our
270 purposes, these line scans cross one or more nuclei (white arrows in Fig. 4A, top row). Pairs of
271 pixels, $\Delta x = 6$ pixels apart, are then correlated over time to calculate the pCF carpet (Fig. 4A,
272 bottom panels). A positive correlation occurs only when a Dl-GFP molecule that is detected in a
273 pixel at position $x = x_1$ and time point t_1 is detected again $\Delta x = 6$ pixels to the right at time point
274 t_2. Statistically, all occurrences of positive correlations starting at x_1 and having a time difference
275 of $\Delta t = t_2 - t_1$ are averaged over 200,000 scans of the line across the nuclei, resulting in a value
276 on the pCF carpet at coordinate $(x_1, \Delta t)$. To ensure robustness of the data, pCF carpets were also
277 calculated for $\Delta x = 7$ or 8 pixels, as well as for pairs of pixels in the right-to-left direction.
278
279 After visual inspection of the pCF carpets, we noticed that pixel locations just to the left of the
280 nuclear membrane aligned with either zero correlation (green bars, Fig. 4A), in which no positive
281 correlation is detected over the time course of the experiment, or delayed correlation (orange
282 arches, Fig. 4A), in which the earliest positive correlations are detected much later compared to
283 other pixel locations. These visual inspections suggested that Dl-GFP molecules in the nucleus
284 either failed to cross the nuclear membrane or could not do so immediately. To quantify this, we
285 calculated the Movement Index (MI) for each embryo, which represents the degree of Dl-GFP
286 movement across the nuclear envelope (see Materials and Methods). A high movement index
287 suggests that Dl-GFP can cross the nuclear envelope, which is represented by an arch in the pCF
288 carpet (demarcated by orange, dashed lines in Fig. 4A). In contrast, a low movement index
289 suggests that Dl-GFP movement into or out of the nucleus is blocked, which is represented by a
290 fully black column in the pCF carpet (demarcated by green, solid lines in Fig. 4A). Note that, as
291 pCF tracks the same molecule twice (Digman & Gratton, 2009; Hinde et al., 2010), the MI
292 correlates with the time scale over which an individual Dl-GFP molecule can exit the nucleus, and
293 is not equivalent to a nuclear export rate constant, which is a measure of average nuclear export.
294
295 We separated our images into two groups, those with high movement (MI > 0.5) and those with
296 low movement (MI ≤ 0.5). We found that Dl-GFP can move into the nucleus across the spatial
297 regions of the embryo, as the ventral, lateral, and dorsal regions all have a majority of images with
298 high MI values (ventral: 92.86%; lateral: 94.44%; dorsal: 100.00%) (Fig. 4B). However, the
299 ventral and lateral regions have significantly fewer images with high MI values when Dl-GFP is
300 measured leaving the nucleus (ventral: 64.29%; lateral: 72.22%; $p<0.07$, Chi-squared test with
301 likelihood ratio), suggesting that Dl-GFP movement out of the nucleus is restricted in the ventral
302 and lateral regions of the embryo (Fig. 4B). In contrast, on the dorsal side of the embryo, almost
303 all the images measuring Dl-GFP movement out of the embryo have high MI values (94.44%). To
304 test whether this restricted movement out of the nucleus may be dependent on Toll signaling, we
305 also performed pCF analysis in $Toll^{10B}$, $Toll^{r4}$, and $pll^{2/7}$mutant lines (Fig. S3A), and similarly

306 found that a lower proportion of images in "ventral-like" mutants have high MI values when Dl-
307 GFP movement is measured out of the nucleus (*Toll*^{10B}: 96.15% in versus 72.73% out; $p<0.05$,
308 Chi-squared test with likelihood ratio) (Fig. 4B). This suggests that the restriction of Dl to exit the
309 nucleus correlates with the spatial gradient in Toll signaling. As Dl/DNA interactions also correlate
310 with Toll signaling, DNA binding may explain our pCF results. For example, it is likely that a Dl-
311 GFP molecule detected by pCF in a ventral nucleus may be bound to DNA initially, implying it
312 will take longer on average to exit the nucleus than a Dl molecule not initially bound to DNA.
313 Therefore, on the ventral side, the time scale on which an individual Dl-GFP molecule exits the
314 nucleus is longer than on the dorsal side (where DNA binding is not happening). This can be true
315 even if the nuclear export rate constants are the same on the ventral side vs the dorsal side. Thus,
316 our pCF results are consistent with a high fraction of immobilized Dl in the nuclei on the ventral
317 side of the embryo.
318
319 **Analysis of *dl* mutant alleles suggests Cact is present in the nuclei**
320 Our results demonstrate that, on the ventral side, a significant fraction of Dl is bound to DNA,
321 while on the dorsal side, that fraction is statistically indistinguishable from zero. This phenomenon
322 raises the question of how Dl, as a transcription factor, would be present in the nucleus, but not
323 bind to DNA. More generally, we ask what mechanism may cause the fraction of Dl bound to
324 DNA to positively correlate with nuclear Dl concentration, when a mechanism consisting solely
325 of saturating biochemical binding interactions predicts the opposite. As the gradient in Dl/DNA
326 interactions is dictated by Toll signaling, we reasoned that, on the ventral side, Dl/DNA binding
327 may be enhanced by phosphorylation of Dl by Toll. Toll phosphorylation of Dl is known to
328 enhance the affinity of Dl for the nucleus (Fig. 5A') (Drier et al., 1999), but its effect on DNA
329 binding is unknown. To test this hypothesis, we made another GFP-fused allele of *dl*, this time
330 with an alanine replacing serine at Dl residue 317 (*dl*^{S317A}-*gfp*). This allele has been shown to have
331 reduced Toll-mediated phosphorylation of Dl (Drier et al., 1999). Because Dl acts as a homodimer,
332 and thus, like *dl*^{R063C}-*gfp*, this allele may be antimorphic (Drier et al., 1999), we used the *nos*-Gal4
333 line to drive the expression of UAS-*dl*^{S317A}-*gfp* (Brand & Perrimon, 1993). As this allele has been
334 shown to drastically reduce the nuclear localization of Dl (Drier et al., 1999), we imaged embryos
335 carrying one copy of this UAS-driven allele and zero copies of wildtype Dl and found that these
336 embryos had no discernible Dl gradient (Fig. S4A). Therefore, to maintain DV polarity so that the
337 ventral and dorsal sides of the embryo could be distinguished, we overexpressed this allele in the
338 background of the BAC recombineered Dl-mGFP construct. We again used the UAS-*dl*^{wt}-*gfp* as a
339 direct wildtype control. As such, if Toll phosphorylation of Dl is responsible for allowing Dl/DNA
340 interactions, then this allele should have reduced DNA binding on the ventral side compared to the
341 wildtype control. However, upon performing ccRICS analysis, we found that the DNA binding of
342 this allele was not statistically distinguishable from the control on the ventral side (Fig. 5B). We
343 note that we cannot completely rule out the hypothesis that Toll signaling has a small effect on
344 Dl/DNA binding, given these embryos expressed the *dl*^{S317A}-*gfp* allele in the background of the
345 BAC recombineered construct.

346
347 Alternatively, we reasoned that, on the dorsal side, Dl in the nuclei may be in complex with Cact,
348 preventing it from binding to DNA (Fig. 5A'''), as suggested by our experimental and modeling
349 work (Al Asafen et al., 2020; O'Connell & Reeves, 2015; Schloop et al., 2025). As Dl/Cact
350 interactions are downstream of Toll signaling, this hypothesis would be consistent with the
351 gradient in Dl/DNA interactions being dictated by Toll signaling. Therefore, we made a GFP-fused
352 *dl* allele that has reduced Cact binding by mutating serine 234 to a proline (dl^{S234P}-*gfp*)(Drier et al.,
353 2000) and as above, to avoid potential antimorphic effects, we used *nos-Gal4* to overexpress the
354 allele. It has been reported that eliminating the Dl/Cact binding results in a weak gradient of Dl,
355 with Dl significantly entering the nuclei on the Dl side of the embryo (Drier et al., 2000). As such,
356 we imaged embryos carrying one copy of UAS-dl^{S234P}-*gfp* without the benefit of the background
357 of the BAC recombineered construct, and found no discernible Dl gradient, similar to the Toll
358 phosphorylation mutant (Fig. S4B). Therefore, to ensure DV polarity of the Dl gradient is
359 maintained, we performed ccRICS on embryos overexpressing this allele in the background of the
360 BAC recombineered Dl-mGFP construct. If the presence of Cact in the dorsal nuclei is responsible
361 for preventing Dl/DNA interactions, then this allele should have increased DNA binding on the
362 dorsal side compared to the wildtype control. Indeed, our ccRICS analysis found that the DNA
363 binding of this allele was greater than the control on the dorsal side (Fig. 5C). The small effect size
364 was likely due to the presence of a wildtype Dl protein in the form of the BAC recombineered Dl-
365 mGFP construct. Indeed, the small effect size may have prevented us from discerning a statistically
366 significant effect of this allele to increase Dl binding on the ventral side (Fig. 5B). Nevertheless,
367 the effect on the dorsal side (Fig. 5C) was statistically significant (p-value $\sim 10^{-3}$). We conclude
368 that the gradient in nuclear Dl mobility is due to Dl/Cact complex in the nucleus; however, we
369 cannot rule out an additional, albeit small, role that Toll phosphorylation may also play. Our
370 previous modeling work has predicted that the presence of Cact in the nucleus affects the spatial
371 range of the Dl gradient and the robustness of gene expression (Al Asafen et al., 2020; O'Connell
372 & Reeves, 2015). Thus, our findings affect the foundation of our understanding of Dl-dependent
373 patterning of the DV axis.
374
375
376 **Discussion**
377 In this study, we used fluorescence fluctuation spectroscopy methods to quantify the movement of
378 a BAC-recombineered, GFP-tagged Dl protein in the 1-3 hr old *Drosophila* embryo (Fig. 5A). Our
379 investigations ultimately unveiled a DV asymmetry in the mobility of Dl, which was correlated to
380 a similar DV asymmetry in the ability of Dl to bind to DNA. First, through RICS analysis, we
381 identified variations in Dl's apparent diffusivity along the DV axis within the nucleus. Given the
382 possibility that at least two pools of Dl exist in the nucleus (free vs immobilized), we built a two-
383 component model that accounts for both pools of Dl and found that the DV asymmetry in the
384 fraction of immobilized Dl explained the DV asymmetry in apparent diffusivity. Therefore, to test
385 whether the observed immobilized Dl could be explained by Dl/DNA binding, we used ccRICS to

386 cross-correlate Dl-GFP with Histone-RFP. We indeed found the DV variations in the fraction of
387 immobilized Dl correlated with Dl/DNA binding, with the highest DNA binding on the ventral
388 side. Moreover, the results obtained from pCF showed that there is also variation in the movement
389 of Dl out of the nuclei: on the ventral side, the propensity of Dl to exit the nucleus is not as rapid
390 as it is on the dorsal side. Taken together, our results suggest that there is a DV asymmetry in the
391 efficiency with which Dl can bind to the DNA, and that the restricted nuclear Dl movement on the
392 ventral side of the embryo is explained by a high proportion of DNA-bound Dl.
393
394 We identified two plausible explanations that could be causing the DV variation in Dl/DNA
395 interactions. First, Toll-mediated phosphorylation of Dl on the ventral side of the embryo might
396 increase its DNA-binding affinity. Indeed, phosphorylated Dl has increased ability to enter the
397 nucleus (Drier et al., 1999, 2000; Gillespie & Wasserman, 1994; Whalen & Steward, 1993).
398 However, no previous evidence has been shown supporting phosphorylated Dl having an increased
399 affinity for DNA. Second, it is possible that nuclear Dl on the dorsal side is predominantly in
400 complex with Cact, which would result in high average mobility, owing to the fact that it cannot
401 bind DNA (Geisler et al., 1992; Kidd, 1992). In support of this explanation, our recent live imaging
402 of an endogenously-tagged Cact showed that, in *Drosophila* embryos, Cact is present in the
403 nucleus (Schloop et al., 2025). In comparison, mammalian IκB, the homolog of Cact, enters the
404 nucleus to regulate NF-κB dimers, which are then rapidly exported from the nuclei (Arenzana-
405 Seisdedos et al., 1995, 1997; Banerjee & Sen, 2006; Carlotti et al., 2000; Hall et al., 2006; Lisiero
406 et al., 2020; Turpin et al., 1999).
407
408 To test these competing hypotheses, we generated two mutant alleles of *dl*, one of which reduced
409 phosphorylation of Dl by Toll (Drier et al., 1999), and the other reduced Dl/Cact interactions (Drier
410 et al., 2000). Using ccRICS, we found that, while the reduced Toll allele exhibited little-to-no
411 change in DNA affinity on the ventral side, the reduced Cact allele did indeed have increased DNA
412 affinity on the dorsal side, consistent with the prediction of the second hypothesis. However, to
413 maintain the DV polarity of the embryo, we expressed these mutant alleles in the background of
414 the BAC recombineered Dl-mGFP construct, such that the effects of these alleles were diluted by
415 the presence of a GFP-tagged wildtype Dl protein. Therefore, while can safely reject the null
416 hypothesis that Cact has no effect on DNA binding, it is possible that our failure to reject the null
417 hypothesis that Toll phosphorylation has no effect on the DNA binding of Dl on the ventral side
418 may be due to this dilution effect.
419
420 Genetically, the bulk of the embryos in this study maternally expressed one copy of endogenous
421 Dl and one copy of the BAC-recombineered construct, which presents two caveats. First, it is
422 known that tagging Dl with a fluorescent protein alters its gradient (Reeves et al., 2012), which
423 may in part be due to a lowered diffusivity (Carrell et al., 2017). As such, any raw diffusivity
424 reported here may measure as slightly lower than that of untagged Dl. We do not expect the fraction
425 immobile or the fraction bound to DNA to be affected. A second caveat is that the presence of

endogenous Dl may increase the variance of our data. As Dl exists as a dimer (Govind et al., 1992; Isoda & Nüsslein-Volhard, 1994), our measurements are likely to reflect an ensemble average of a tagged/untagged heterodimer mixed with a tagged homodimer at a 2:1 ratio. We do not expect the existence of a mixed population of Dl dimers to alter our main conclusions.

It is thought that the primary role for Cact is to tether Dl to the cytoplasm and prevent nuclear translocation. Indeed, loss of Cact function permits intermediate levels of Dl to enter the nuclei, even on the dorsal side of the embryo (Bergmann et al., 1996; Cardoso et al., 2017; Roth et al., 1991). However, recent studies have discovered multiple functions for Cact, including positive roles in the formation of the Dl gradient. For example, Cact degradation on the ventral side of the embryo creates a driving force for a ventrally-directed net flux of Dl/Cact complex, which has the overall effect of shuttling Dl to the ventral side (Carrell et al., 2017). Furthermore, recent experimental and modeling work has suggested that Cact potentiates nuclear translocation on the ventral side of the embryo (Barros et al., 2021; Cardoso et al., 2017).

In addition to these roles for Cact in establishing the Dl gradient, our experimental results in this study suggest that, on the dorsal side of the embryo, Cact is present inside the nuclei and plays a role in preventing Dl from binding DNA. While this specific finding relates to the dorsal half of the embryo, where Dl levels are low and are expected to have minimal activity in regulating gene expression, knowing whether Dl is in complex with Cact in the dorsal-most nuclei is crucial to our understanding of the Dl gradient. Indeed, our previous fluorescence measurements have revealed a gradient that decays to non-zero basal levels on the dorsal half of the embryo (Liberman et al., 2009; Reeves et al., 2012); such a gradient would have a very limited dynamic range, varying by less than one order of magnitude (O'Connell & Reeves, 2015). In light of our results in this paper, one solution to this problem is to assume all of the Dl on the dorsal side of the embryo is Dl/Cact complex, meaning that the gradient of free Dl would have an unknown overall shape, but would decay to near-zero levels. We have shown that such a free Dl gradient would not only have extended spatial and dynamic ranges, but also superior precision and robustness of gene expression compared to the gradient measured by fluorescence (Al Asafen et al., 2020; Liberman et al., 2009; O'Connell & Reeves, 2015; Reeves et al., 2012). In support of the assumption that all Dl is bound to Cact on the dorsal side, we have recently shown that Cact exhibits dynamics similar to Dl on the dorsal side of the embryo, suggesting that, in both cases, it is predominantly Dl/Cact complex that is being measured (Hiremath et al., 2024; Reeves et al., 2012; Schloop et al., 2025).

Furthermore, our recent experimental work showed that Cact is present in all nuclei and is spatially uniform along the DV axis of the embryo (Schloop et al., 2025). As such, our results in this paper can likely be extended to Dl/Cact interactions in all nuclei, implying that measurements of the Dl gradient based solely on nuclear fluorescence levels are in fact a combination of a spatially graded pool of free (active) Dl and a spatially uniform level of Dl/Cact complex along the entire DV axis. Thus, the "true" Dl activity gradient remains unquantified, and must be determined by

466 deconvolving Dl/Cact complex from free Dl (O'Connell & Reeves, 2015). If all (or nearly all) of
467 the Dl in the dorsal-most nuclei is indeed bound by Cact, the gradient of free Dl, along the entire
468 DV axis, could be recovered by simply subtracting off the basal levels. However, it is likely that
469 some fraction of Dl in the dorsal-most nuclei is free. Thus, to fully understand the positional
470 information carried by the Dl gradient, direct quantification of Dl/Cact complex, perhaps through
471 ccRICS measurements on embryos in which both Dl and Cact are labeled, should be the next step
472 towards gaining future insights into the operation of the highly conserved NF-κB/Dl module.
473 Ultimately, our work highlights the need for quantitative measurements of biophysical parameters
474 to further our understanding of signaling and gene expression, and calls for similar studies in other
475 signaling pathways in embryonic patterning.
476
477
478
479 **Materials and Methods**
480
481 **Fly Stocks and Preparation**
482 *Drosophila melanogaster* stocks were kept on corn meal molasses food in vials or bottles at 25°C
483 and all crosses were performed at 25°C. *Drosophila* embryos, that were about 1-2 hrs old, were
484 collected and mounted on slides for imaging. Briefly, flies were left to deposit eggs on fresh grape
485 juice agar plates with yeast paste for 30-60 min. Those embryos were then aged further for 30 min
486 at 25°C to reach the desired developmental stage. Those embryos are then brushed from the grape
487 juice agar plates into a mesh basket using a paintbrush and DI water. The embryos were
488 dechorionated using bleach and then washed with DI water (Carrell & Reeves 2009).
489
490 *dl-mGFP* (Dl-GFP) was created by BAC recombineering and $dl^{1.2.5}$ flies were generated by
491 cleaning up dl^{1} via two homologous recombinations with wildtype flies (Carrell et al. 2017). Flies
492 carrying $dl^{1.2.5}$ were crossed to flies carrying H2Av-RFP on the second chromosome (w[*];
493 P{w[+mC]=His2Av-mRFP1}II.2; BS# 23651) to generate flies that have $dl^{1.2.5}$,H2Av-RFP
494 transgene on the second chromosome. H2Av-RFP,$dl^{1.2.5}$,*dl-mGFP* flies were created by
495 homologous recombination (Carrell et al. 2017). Thus, the "Dl-GFP embryos" analyzed in this
496 study had a maternal genotype of H2Av-RFP,$dl^{1.2.5}$,*dl-mGFP*/*CyO*: one copy of endogenous *dl*
497 and one copy of *dl-mGFP*. The generation of $Toll^{r4}$ and $Toll^{10B}$ mutant embryos has been
498 previously described (Stathopoulos et al. 2002). Other *Drosophila* strains were obtained from the
499 Bloomington (BL) stock center, namely pll^{2} (e[1] pll[2] ca[1]/TM3, Sb[1] BS# 3111) and pll^{7} (e[1]
500 pll[7] ca[1]/TM3, Sb[1]; BS# 3112), and nos-Gal4 (w[1118]; P{w[+mC]=GAL4::VP16-
501 nanos.UTR}CG6325[MVD1]; BS# 4937).
502
503 The pUAST plasmids containing *dl* alleles (dl^{wt}-*mgfp*, dl^{R063C}-*mgfp*, dl^{S317A}-*mgfp*, and dl^{S234P}-
504 *mgfp*) were prepared by site-directed mutagenesis using appropriate primers with the Q5® Site-
505 Directed Mutagenesis Kit (New England Biolabs Inc., Frankfurt, Germany). All resulting plasmids
506 were confirmed by direct sequencing. The Gal4/UAS overexpression embryos were maternally

507 H2Av-RFP,*dl*^{1,2,5},*dl-mGFP*/*dl*^{4}; *nos*-Gal4/UAS-*dl*^{x}-*mGFP*, where *x* is either the R063C, S317A,
508 or S234P mutation, or wildtype. Thus, these embryos maternally carried zero endogenous copies
509 of *dl*, one BAC-recombineered *dl-mGFP* construct, and one UAS-*dl*^{x}-*mGFP* construct.
510
511 **Fly Transformation**
512 *Drosophila* embryos were injected with 0.5 ng/µl of each pUAST construct using the PhiC31
513 method by GenetiVision (Texas, USA). Transformed flies include insertion on chromosome III.
514 Stocks were established for each of these flies. The flies were then crossed into a dl^{4} heterozygous
515 background (dl[4] pr[1] cn[1] wx[wxt] bw[1]/CyO BS# 7096) and finally crossed with dl1.2.5 flies
516 (Carrell et al., 2017) driven by nos-gal4 (BS# 4937, see above). The females from this cross were
517 kept in a cage and the resulting embryos were used for live imaging.
518
519 **Mounting and Imaging of *Drosophila* Embryos**
520 *Drosophila* embryos that were 1-2 hrs old were mounted laterally on a microscope slide using a
521 mixture of heptane glue (Supatto et al. 2009) and two pieces of double-sided tape to prevent sample
522 movement (Carrell & Reeves 2015). The embryos were mounted in random orientations along the
523 DV axis. The DV position of each imaged region was estimated by measuring the Dl nuclear-to-
524 cytoplasmic ratio (NCR) of intensity, which varies predictably with position along the DV axis.
525 We categorized positions with NCRs > 1.25 as ventral, positions with 0.75 < NCR < 1.25 as lateral,
526 and positions with NCR < 0.75 as dorsal (Fig. 1A). Embryos were imaged on either a Zeiss LSM
527 710 or LSM 900 confocal microscope using a 40x 1.2NA water objective. Embryos in nuclear
528 cycle 12 to 14 were selected using the H2Av-RFP marker. Embryos undergoing cell division (as
529 visualized by the H2Av-RFP marker) were not used in for analysis as cell division alters the
530 endogenous Dl distribution.
531
532 For image acquisition consistent with RICS analysis for the data shown in Figs. 1-3, using a Zeiss
533 LSM 710, a 256 x 256 pixel region of interest of the embryo was selected for measurements
534 (Supplemental Figure 1). The pixel size of the region varied from 40 nm to 100 nm to include
535 different numbers of nuclei. The 25 mW 488 nm laser intensity ranged from 0.5% to 3.0% and the
536 20 mW 570 nm laser intensity ranged from 0.1% to 0.2%. The region of interest was raster scanned
537 with a pixel dwell time of 6.3 µs for 200 frames (total imaging time of approximately 1.5 minutes).
538 For dl-mutants (data shown in Fig. 5) we used Zeiss LSM 900 with a 1024 x 1024 pixel region of
539 interest, with a pixel size of 30 nm (Supplemental Figure 1), having the laser intensity range same
540 as mentioned above for the 10 mW 488 nm laser and the 10 mW 561 nm laser. The region of
541 interest was raster scanned with a pixel dwell time of 2.1 µs for 100 frames (total imaging time of
542 approximately 9 min). The range of imaging parameters is reported in Table S1.
543
544 For image acquisition consistent with pCF analysis, a 32x1 line scan through 2 to 4 nuclei was
545 used as the region of interest (Fig. 4A). The pixel size was not set for each image but, instead,
546 varied between 40-100nm according to the region of interest selected. The laser intensities varied

as in the RICS imaging. The line was scanned with a pixel dwell time of 6.30μs for 200,000 to 400,000 time points (total imaging time of approximately 1.5 to 3 minutes). The range of imaging parameters is reported in Table S1.

Raster Image Correlation Spectroscopy (RICS) analysis using MATLAB implementation

RICS analysis of time series images is briefly described here (see Supplemental Information for more details). For each frame j (of size 256×256 or 1024x1024 pixels) in the Dl-GFP channel, the scanning ACF, $G_j(\xi,\eta)$, was computed according to the following for all pixel shifts ξ,η:

$$G_j(\xi,\eta) = \frac{\langle I_j(x,y) I_j(x+\xi, y+\eta)\rangle}{\langle I_j(x,y)\rangle^2} - 1, \qquad (1)$$

where $I_j(x,y)$ is the intensity of frame j at pixel coordinates (x,y) and the angle brackets denote ensemble average in both x and y. In practice, $G_j(\xi,\eta)$ is evaluated using the fast Fourier transform method (Digman & Gratton, 2011). The final ACF for total RICS, $G_s(\xi,\eta)$, was computed as the average of $G_j(\xi,\eta)$ for all frames j in the time series. Cross-correlation functions were computed in a similar way, except $I_j(x+\xi, y+\eta)$ was replaced by the analogous array from the H2Av-RFP channel, and the $\langle I_j(x,y)\rangle^2$ in the denominator was replaced by the product of the average intensity in the Dl-GFP channel and the average intensity in the H2Av-RFP channel.

Fitting models to the ACFs

The one component diffusion model for the RICS ACF is (Fig. 1D-F; Digman et al., 2005b):

$$G_s^{1c}(\xi,\eta; A,B,D,w_0) = \frac{(A-B)\exp\left(-\frac{(r/w_0)^2}{1+4D\,\tau/w_0^2}\right)}{(1+4D\,\tau/w_0^2)\sqrt{1+4D\,\tau/w_z^2}} + B, \qquad (2)$$

where $r = \Delta r\sqrt{\xi^2+\eta^2}$, $\tau = \tau_p\xi + \tau_\ell\eta$, Δr is the pixel size in microns, τ_p and τ_ℓ are the pixel dwell time and line scan time in seconds, respectively, and w_0 and w_z are the waist sizes of the point spread function in the planar and axial directions, respectively. The two component diffusion/binding model is a linear combination of two instances of Equation (2):

$$G_s^{2c}(\xi,\eta; A,B,\phi,w_0) = (A-B)[\phi G_s^{1c}(\xi,\eta; 1,0,0,w_0) + (1-\phi)G_s^{1c}(\xi,\eta; 1,0,3,w_0)] + B, \qquad (3)$$

where ϕ is the fraction of Dl-GFP that is immobilized, in the first term, D is held fixed at zero, and in the second term, D is held fixed at 3 μm^2/s. Within both terms, G_s^{1c} is normalized such that $A = 1$ and $B = 0$, because the A and B parameters are otherwise present in Equation (3).

Models of the ACF were fit to the ACFs calculated from the total, nuclear, or cytoplasmic data in two steps. First, the fast direction of the ACF ($\eta = 0$) was used as target to fit $G_s^{1c}(\xi, 0; A, B, 0, w_0)$, that is, Equation (2) with $\eta = 0$ and $D = 0$. The shape of this function is purely Gaussian and

583 approximates the point spread function (PSF). This fit is highly robust, and performing this fit first
584 allows for accurate estimation of the parameter A. Two parameters, the PSF waist size, w_0, and
585 the background level, B, are theoretically fixed; however, we allowed them to vary slightly from
586 their theoretical values of 0.25 μm and zero, respectively, for robustness of fit.
587
588 In the second step, with A from the first step fixed, either Equation (2), for the one-component
589 model, or Equation (3), for the two component model, was fit to $G_s(\xi,\eta)$ using least squares and
590 varying B, D, w_0 or B, ϕ, w_0 , respectively. The parameters $\Delta r, \tau_p, \tau_\ell, w_z$ were microscope
591 parameters and considered fixed. More information can be found in the Supplemental Information.
592
593 **Pair Correlation Function (pCF) analysis using SimFCS software**
594 Acquisitions were taken of 200,000 scans of a line 32 pixels across (pixel size 0.5 μm), with a
595 pixel dwell time of 6.3 μs and a line time of 0.47 ms, on either the dorsal, lateral, or ventral sides
596 of nc 14 embryos. To ensure minimal movement of nuclei occurred during the line scan aquisition,
597 512x512 images were taken before and after each acquisition, where the middle y-coordinate of
598 these images corresponded to the location of the line scan (white arrows in Fig. 4A). pCF analysis
599 of the collected line scans was performed using the SimFCS software (Digman et al, 2005;
600 https://www.lfd.uci.edu/globals/) as described in Clark and Sozzani, 2017. Three pixel distances
601 of 6, 7, and 8 pixels were used as technical replicates to account for differences in sizes of nuclei.
602 If Dl-GFP showed movement out of/into a majority of nuclei (no black region or black arch in the
603 pCF carpet), that image was assigned a movement index of 1. Otherwise, if the majority of Dl-
604 GFP showed no movement (black vertical region in the pCF carpet), that image was assigned a
605 movement index of 0 (Fig. 4A). The 3 technical replicates were then averaged for each biological
606 replicate. The analysis was repeated for the line scan in the reverse direction, resulting in 6 total
607 technical replicates per image.
608
609 **Quantification and statistical analysis**
610 Non-linear least squares was used to fit Equation (2) to the RICS ACFs. The fitted diffusivity value
611 is *t*-distributed, and a standard error for the diffusivity (radius of a 68% confidence interval) was
612 calculated. With the exception of five time course image stacks of nuclear RICS either on the
613 dorsal side of wildtype embryos, or in $pll^{2/7}$ embryos (the two cases in which nuclear intensity is
614 very low), for all fitted diffusivities, the standard error was less than 4 $\mu m^2/s$. This was used as a
615 filter for the data; the five time course image stacks in which the standard error was greater than 4
616 $\mu m^2/s$ were removed from the analysis.
617
618 For the diffusivity of Dl calculated by RICS (Fig. 1D-F), the ccRICS data (ratio of amplitudes;
619 Fig. 3C,D), and for the correlation between nuclear diffusivity and φ (Fig. 4E), simple linear least
620 squares regression was applied. The slope of the regression trend line is t-distributed with n-2
621 degrees of freedom, where n is the number of data points. Reported *p*-values are for *t*-tests with
622 the null hypothesis that the slope is zero.

For the pCF data (Fig. 2), a Chi-squared test with likelihood ratio was used to test if the proportion of Movement Index (MI) values that were less than 0.5 was different for movement measured into the nucleus vs movement measured out of the nucleus. The Chi-squared test was performed using JMP software (https://www.jmp.com/).

For all tests, a p-value less than 0.05 was considered significant, and for the Chi-Squared test we also consider the two p-values that were less than 0.07 as significant (Fig. 2). The statistical tests performed on each sample are listed in the Results text as well as the figure legends. Sample sizes are indicated in the figures. Means and standard errors are reported in the Results.

Data and software availability

Images, tables, and sequencing results will be uploaded to a data repository, Data Dryad. Accession numbers will be available upon notification of acceptance for publication. Matlab codes will be uploaded to github and will also be available from the Reeves Lab website.

Acknowledgements

The authors acknowledge the use of the Cellular and Molecular Imaging Facility (CMIF) at North Carolina State University, which is supported by the State of North Carolina and the National Science Foundation.

References

Al Asafen, H., Bandodkar, P. U., Carrell-Noel, S., Schloop, A. E., Friedman, J., & Reeves, G. T. (2020). Robustness of the Dorsal morphogen gradient with respect to morphogen dosage. *PLOS Computational Biology*, *16*(4), e1007750. https://doi.org/10.1371/journal.pcbi.1007750

Anderson, K. V, Bokla, L., & Nüsslein-Volhard, C. (1985). Establishment of dorsal-ventral polarity in the Drosophila embryo: the induction of polarity by the Toll gene product. *Cell*, *42*(3), 791–798. https://doi.org/10.1016/0092-8674(85)90275-2

Anderson, K. V, Jürgens, G., & Nüsslein-Volhard, C. (1985). Establishment of dorsal-ventral polarity in the Drosophila embryo: Genetic studies on the role of the Toll gene product. *Cell*, *42*(3), 779–789. https://doi.org/http://dx.doi.org/10.1016/0092-8674(85)90274-0

Anderson, K. V, & Nüsslein-Volhard, C. (1984). Information for the dorsal--ventral pattern of the Drosophila embryo is stored as maternal mRNA. *Nature*, *311*(5983), 223–227. https://doi.org/10.1038/311223a0

Arenzana-Seisdedos, F., Thompson, J., Rodriguez, M. S., Bachelerie, F., Thomas, D., & Hay, R. T. (1995). Inducible nuclear expression of newly synthesized I kappa B alpha negatively regulates DNA-binding and transcriptional activities of NF-kappa B. *Mol Cell Biol*, *15*(5), 2689–2696. http://mcb.asm.org/content/15/5/2689.abstract

Arenzana-Seisdedos, F., Turpin, P., Rodriguez, M., Thomas, D., Hay, R. T., Virelizier, J. L., & Dargemont, C. (1997). Nuclear localization of I kappa B alpha promotes active transport of NF-kappa B from the nucleus to the cytoplasm. *J Cell Sci*, *110*, 369–378. http://jcs.biologists.org/content/110/3/369.abstract

Banerjee, D., & Sen, R. (2006). Cellular Dynamics of NF-κB Associated Proteins. In *NF-κB/Rel Transcription Factor Family* (pp. 41–50). Springer US. https://doi.org/10.1007/0-387-33573-0_4

Barros, C. D. T., Cardoso, M. A., Bisch, P. M., Araujo, H. M., & Lopes, F. J. P. (2021). A reaction-diffusion network model predicts a dual role of Cactus/IκB to regulate Dorsal/NFκB nuclear translocation in Drosophila. *PLOS Computational Biology*, *17*(5), e1009040. https://doi.org/10.1371/journal.pcbi.1009040

Belvin, M. P., & Anderson, K. V. (1996). A Conserved Signalig Pathway: The Drosophila Toll-Dorsal Pathway. *Annual Review of Cell and Developmental Biology*, *12*(1), 393–416. https://doi.org/10.1146/annurev.cellbio.12.1.393

Belvin, M. P., Jin, Y., & Anderson, K. V. (1995). Cactus protein degradation mediates Drosophila dorsal-ventral signaling. *Genes Dev*, *9*(7), 783–793. http://www.genesdev.org/cgi/reprint/9/7/783

Bergmann, A., Stein, D., Geisler, R., Hagenmaier, S., Schmid, B., Fernandez, N., Schnell, B., & Nüsslein-Volhard, C. (1996). A gradient of cytoplasmic Cactus degradation establishes the nuclear localization gradient of the dorsal morphogen in Drosophila. *Mechanisms of Development*, *60*(1), 109–123. http://www.ncbi.nlm.nih.gov/pubmed/9025065

Brand, A. H., & Perrimon, N. (1993). Targeted gene expression as a means of altering cell fates and generating dominant phenotypes. *Development*, *118*(2), 401–415.

Cardoso, M. A., Fontenele, M., Lim, B., Bisch, P. M., Shvartsman, S. Y., & Araujo, H. M. (2017). A novel function for the IκB inhibitor Cactus in promoting Dorsal nuclear localization and activity in the Drosophila embryo. *Development*, *144*(16), 2907–2913. https://doi.org/10.1242/dev.145557

Carlotti, F., Dower, S. K., & Qwarnstrom, E. E. (2000). Dynamic Shuttling of Nuclear Factor κB between the Nucleus and Cytoplasm as a Consequence of Inhibitor Dissociation. *Journal of Biological Chemistry*, *275*(52), 41028–41034. https://doi.org/10.1074/jbc.M006179200

Carrell, S. N., Connell, M. D. O., Jacobsen, T., Pomeroy, A. E., Hayes, S. M., & Reeves, G. T. (2017). A facilitated diffusion mechanism establishes the Drosophila Dorsal gradient. *Development*, *144*(23), 4450–4461. https://doi.org/10.1242/dev.155549

Chopra, V. S., & Levine, M. (2009). Combinatorial patterning mechanisms in the Drosophila embryo. *Briefings in Functional Genomics & Proteomics*, *8*(4), 243–249. https://doi.org/10.1093/bfgp/elp026

Daigneault, J., Klemetsaune, L., & Wasserman, S. A. (2013). The IRAK homolog Pelle is the functional counterpart of IκB kinase in the Drosophila Toll pathway. *PLoS One*, *8*(9), e75150. https://doi.org/10.1371/journal.pone.0075150

Delotto, R., Delotto, Y., Steward, R., & Lippincott-schwartz, J. (2007). Nucleocytoplasmic shuttling mediates the dynamic maintenance of nuclear Dorsal levels during Drosophila embryogenesis. *Development*, *4241*, 4233–4241. https://doi.org/10.1242/dev.010934

Digman, M. A., Brown, C. M., Sengupta, P., Wiseman, P. W., Horwitz, A. R., & Gratton, E. (2005). Measuring fast dynamics in solutions and cells with a laser scanning microscope. *Biophys J*, *89*(2), 1317–1327. https://doi.org/10.1529/biophysj.105.062836

Digman, M. A., & Gratton, E. (2009). Imaging barriers to diffusion by pair correlation functions. *Biophys J*, *97*(2), 665–673. https://doi.org/10.1016/j.bpj.2009.04.048

Digman, M. A., & Gratton, E. (2011). Lessons in fluctuation correlation spectroscopy. *Annual Review of Physical Chemistry*, *62*, 645–668. https://doi.org/10.1146/annurev-physchem-032210-103424

Digman, M. A., Sengupta, P., Wiseman, P. W., Brown, C. M., Horwitz, A. R., & Gratton, E. (2005). Fluctuation correlation spectroscopy with a laser-scanning microscope: exploiting the hidden time structure. *Biophys J*, *88*(5), L33--L36. https://doi.org/10.1529/biophysj.105.061788

Digman, M. A., Wiseman, P. W., Horwitz, A. R., & Gratton, E. (2009). Detecting protein complexes in living cells from laser scanning confocal image sequences by the cross correlation raster image spectroscopy method. *Biophys J*, *96*(2), 707–716. https://doi.org/10.1016/j.bpj.2008.09.051

Drier, E. A., Govind, S., & Steward, R. (2000). Cactus-independent regulation of Dorsal nuclear import by the ventral signal. *Current Biology : CB*, *10*(1), 23–26. https://doi.org/10.1016/S0960-9822(99)00267-5

Drier, E. A., Huang, L. H., & Steward, R. (1999). Nuclear import of the Drosophila Rel protein Dorsal is regulated by phosphorylation. *Genes & Development*, *13*(5), 556–568. https://doi.org/10.1101/gad.13.5.556

Entchev, E. V, Schwabedissen, A., & González-Gaitán, M. A. (2000). Gradient formation of the {TGF}-beta homolog {D}pp. *Cell*, *103*(6), 981–991. https://doi.org/10.1016/S0092-8674(00)00200-2

Geisler, R., Bergmann, A., Hiromi, Y., & Nüsslein-Volhard, C. (1992). cactus, a gene involved in dorsoventral pattern formation of Drosophila, is related to the I kappa B gene family of vertebrates. *Cell*, *71*(4), 613–621. https://doi.org/10.1016/0092-8674(92)90595-4

Gillespie, S. K., & Wasserman, S. A. (1994). Dorsal, a Drosophila Rel-like protein, is phosphorylated upon activation of the transmembrane protein Toll. *Molecular and Cellular Biology*, *14*(6), 3559–3568. https://doi.org/10.1128/MCB.14.6.3559

Govind, S., Drier, E., Huang, L. H., & Steward, R. (1996). Regulated nuclear import of the Drosophila rel protein dorsal: structure-function analysis. *Molecular and Cellular Biology*, *16*(3), 1103–1114. http://www.pubmedcentral.nih.gov/articlerender.fcgi?artid=231093&tool=pmcentrez&rendertype=abstract

Govind, S., Whalen, A. M., & Steward, R. (1992). In vivo self-association of the Drosophila rel-protein dorsal. *Proceedings of the National Academy of Sciences of the United States of America*, *89*(17), 7861–7865. http://www.pubmedcentral.nih.gov/articlerender.fcgi?artid=49814&tool=pmcentrez&rendertype=abstract

Gregor, T., Wieschaus, E. F., McGregor, A. P., Bialek, W., & Tank, D. W. (2007). Stability and nuclear dynamics of the Bicoid morphogen gradient. *Cell*, *130*(1), 141–152. https://doi.org/10.1016/j.cell.2007.05.026

Hall, G., Hasday, J. D., & Rogers, T. B. (2006). Regulating the regulator: NF-κB signaling in heart. *Journal of Molecular and Cellular Cardiology*, *41*(4), 580–591. https://doi.org/10.1016/j.yjmcc.2006.07.006

Hinde, E., Cardarelli, F., Digman, M. A., & Gratton, E. (2010). In vivo pair correlation analysis of EGFP intranuclear diffusion reveals DNA-dependent molecular flow. *Proc Natl Acad Sci U S A*, *107*(38), 16560–16565. https://doi.org/10.1073/pnas.1006731107

Hiremath, S. V., Goyal, E., Reeves, G. T., & Williams, C. M. (2024). FRAP analysis: Measuring biophysical kinetic parameters using image analysis. *ArXiv*. https://doi.org/10.48550/arXiv.2402.16615

Holzer, T., Liffers, K., Rahm, K., Trageser, B., Özbek, S., & Gradl, D. (2012). Live imaging of

active fluorophore labelled Wnt proteins. *FEBS Letters*, *586*(11), 1638–1644. https://doi.org/10.1016/j.febslet.2012.04.035

Isoda, K., & Nüsslein-Volhard, C. (1994). Disulfide cross-linking in crude embryonic lysates reveals three complexes of the Drosophila morphogen dorsal and its inhibitor cactus. *Proc Natl Acad Sci U S A*, *91*(12), 5350–5354. http://www.pnas.org/content/91/12/5350.abstract

Isoda, K., Roth, S., & Nüsslein-Volhard, C. (1992). The functional domains of the Drosophila morphogen dorsal: evidence from the analysis of mutants. *Genes Dev*, *6*(4), 619–630. http://genesdev.cshlp.org/cgi/content/abstract/6/4/619

Kidd, S. (1992). Characterization of the Drosophila cactus locus and analysis of interactions between cactus and dorsal proteins. *Cell*, *71*(4), 623–635. http://www.ncbi.nlm.nih.gov/pubmed/1423619

Liberman, L. M., Reeves, G. T., & Stathopoulos, A. (2009). Quantitative imaging of the Dorsal nuclear gradient reveals limitations to threshold-dependent patterning in Drosophila. *Proceedings of the National Academy of Sciences of the United States of America*, *106*(52), 22317–22322. https://doi.org/10.1073/pnas.0906227106

Lisiero, D. N., Cheng, Z., Tejera, M. M., Neldner, B. T., Warrick, J. W., Wuerzberger-Davis, S. M., Hoffmann, A., Suresh, M., & Miyamoto, S. (2020). IκBα Nuclear Export Enables 4-1BB–Induced cRel Activation and IL-2 Production to Promote CD8 T Cell Immunity. *The Journal of Immunology*, *205*(6), 1540–1553. https://doi.org/10.4049/jimmunol.2000039

Luz, M., Spannl-Müller, S., Özhan, G., Kagermeier-Schenk, B., Rhinn, M., Weidinger, G., & Brand, M. (2014). Dynamic Association with Donor Cell Filopodia and Lipid-Modification Are Essential Features of Wnt8a during Patterning of the Zebrafish Neuroectoderm. *PLoS ONE*, *9*(1), e84922. https://doi.org/10.1371/journal.pone.0084922

Moussian, B., & Roth, S. (2005). Dorsoventral axis formation in the Drosophila embryo--shaping and transducing a morphogen gradient. *Curr. Biol.*, *15*(21), R887--R899. https://doi.org/10.1016/j.cub.2005.10.026

O'Connell, M. D., & Reeves, G. T. (2015). The Presence of Nuclear Cactus in the Early Drosophila Embryo May Extend the Dynamic Range of the Dorsal Gradient. *PLOS Computational Biology*, *11*(4), e1004159. https://doi.org/10.1371/journal.pcbi.1004159

Reach, M., Galindo, R. L., Towb, P., Allen, J. L., Karin, M., & Wasserman, S. A. (1996). A gradient of cactus protein degradation establishes dorsoventral polarity in the Drosophila embryo. *Dev. Biol.*, *180*(1), 353–364. https://doi.org/10.1006/dbio.1996.0308

Reeves, G. T., & Stathopoulos, A. (2009). Graded dorsal and differential gene regulation in the Drosophila embryo. *Cold Spring Harb Perspect Biol*, *1*(4), a000836. https://doi.org/10.1101/cshperspect.a000836

Reeves, G. T., Trisnadi, N., Truong, T. V, Nahmad, M., Katz, S., & Stathopoulos, A. (2012). Dorsal-ventral gene expression in the Drosophila embryo reflects the dynamics and precision of the dorsal nuclear gradient. *Developmental Cell*, *22*(3), 544–557. https://doi.org/10.1016/j.devcel.2011.12.007

Ribes, V., Balaskas, N., Sasai, N., Cruz, C., Dessaud, E., Cayuso, J., Tozer, S., Yang, L. L., Novitch, B., Marti, E., & Briscoe, J. (2010). Distinct Sonic Hedgehog signaling dynamics specify floor plate and ventral neuronal progenitors in the vertebrate neural tube. *Genes & Development*, *24*(11), 1186–1200. https://doi.org/10.1101/gad.559910

Rippe, K. (2000). Simultaneous Binding of Two DNA Duplexes to the NtrC−Enhancer Complex Studied by Two-Color Fluorescence Cross-Correlation Spectroscopy. *Biochemistry*, *39*(9), 2131–2139. https://doi.org/10.1021/bi9922190

Roth, S., Hiromi, Y., Godt, D., & Nüsslein-Volhard, C. (1991). cactus, a maternal gene required for proper formation of the dorsoventral morphogen gradient in Drosophila embryos. *Development*, *112*(2), 371–388. http://dev.biologists.org/cgi/reprint/112/2/371

Roth, S., Stein, D., & Nüsslein-Volhard, C. (1989). A gradient of nuclear localization of the dorsal protein determines dorsoventral pattern in the Drosophila embryo. *Cell*, *59*(6), 1189–1202. https://doi.org/10.1016/0092-8674(89)90774-5

Schloop, A. E., Bandodkar, P. U., & Reeves, G. T. (2020). Formation, interpretation, and regulation of the Drosophila Dorsal/NF-κB gradient. In *Current Topics in Developmental Biology* (Vol. 137, pp. 143–191). https://doi.org/10.1016/bs.ctdb.2019.11.007

Schloop, A. E., Carrell-Noel, S., Friedman, J., Thomas, A., & Reeves, G. T. (2020). Mechanism and implications of morphogen shuttling: Lessons learned from dorsal and Cactus in Drosophila. *Developmental Biology*. https://doi.org/10.1016/j.ydbio.2020.01.011

Schloop, A. E., Hiremath, S. V., Shaikh, R., Dima, S. S., Lizardo, L., Bhakta, A., Williams, C. M., & Reeves, G. T. (2025). Spatiotemporal dynamics of NF-κB/Dorsal inhibitor IκBα/Cactus in Drosophila blastoderm embryos. *IScience*, *28*(7), 112854. https://doi.org/10.1016/j.isci.2025.112854

Schneider, D. S., Hudson, K. L., Lin, T. Y., & Anderson, K. V. (1991). Dominant and recessive mutations define functional domains of Toll, a transmembrane protein required for dorsal-ventral polarity in the Drosophila embryo. *Genes & Development*, *5*(5), 797–807. https://doi.org/10.1101/gad.5.5.797

Stathopoulos, A., & Levine, M. (2002). Dorsal gradient networks in the Drosophila embryo. *Developmental Biology*, *246*(1), 57–67. https://doi.org/10.1006/dbio.2002.0652

Stathopoulos, A., & Levine, M. (2004). Whole-genome analysis of Drosophila gastrulation. *Curr. Opin. Genet. Dev.*, *14*(5), 477–484. https://doi.org/10.1016/j.gde.2004.07.004

Steward, R. (1987). Dorsal, an embryonic polarity gene in Drosophila, is homologous to the vertebrate proto-oncogene, c-rel. *Science*, *238*(4827), 692–694. http://www.sciencemag.org/content/238/4827/692.short

Steward, R., Zusman, S. B., Huang, L. H., & Schedl, P. (1988). The dorsal protein is distributed in a gradient in early drosophila embryos. *Cell*, *55*(3), 487–495. https://doi.org/10.1016/0092-8674(88)90035-9

Teleman, A. A., & Cohen, S. M. (2000). Dpp gradient formation in the Drosophila wing imaginal disc. *Cell*, *103*(6), 971–980. https://doi.org/10.1016/S0092-8674(00)00199-9

Turpin, P., Hay, R. T., & Dargemont, C. (1999). Characterization of IκBα Nuclear Import Pathway. *Journal of Biological Chemistry*, *274*(10), 6804–6812. https://doi.org/10.1074/jbc.274.10.6804

Wallkamm, V., Dörlich, R., Rahm, K., Klessing, T., Nienhaus, G. U., Wedlich, D., & Gradl, D. (2014). Live Imaging of Xwnt5A-ROR2 Complexes. *PLoS ONE*, *9*(10), e109428. https://doi.org/10.1371/journal.pone.0109428

Wartlick, O., Mumcu, P., Kicheva, A., Bittig, T., Seum, C., Jülicher, F., & González-Gaitán, M. (2011). Dynamics of Dpp signaling and proliferation control. *Science*, *331*(6021), 1154–1159. https://doi.org/10.1126/science.1211373

Weidemann, T., Wachsmuth, M., Tewes, M., Rippe, K., & Langowski, J. (2002). Analysis of Ligand Binding by Two-Colour Fluorescence Cross-Correlation Spectroscopy. *Single Molecules*, *3*(1), 49–61. https://doi.org/10.1002/1438-5171(200204)3:1<49::AID-SIMO49>3.0.CO;2-T

Whalen, A. M., & Steward, R. (1993). Dissociation of the Dorsal-Cactus complex and

phosphorylation of the Dorsal protein correlate with the nuclear localization of Dorsal. *J Cell Biol*, *123*(3), 523–534. http://www.jcb.org/cgi/reprint/123/3/523

Williams, P. H., Hagemann, A., González-Gaitán, M., & Smith, J. C. (2004). Visualizing long-range movement of the morphogen Xnr2 in the Xenopus embryo. *Curr Biol*, *14*(21), 1916–1923. https://doi.org/10.1016/j.cub.2004.10.020

Zhou, S., Lo, W.-C., Suhalim, J. L., Digman, M. A., Gratton, E., Nie, Q., & Lander, A. D. (2012). Free Extracellular Diffusion Creates the Dpp Morphogen Gradient of the Drosophila Wing Disc. *Current Biology*, *22*(8), 668–675. https://doi.org/10.1016/j.cub.2012.02.065

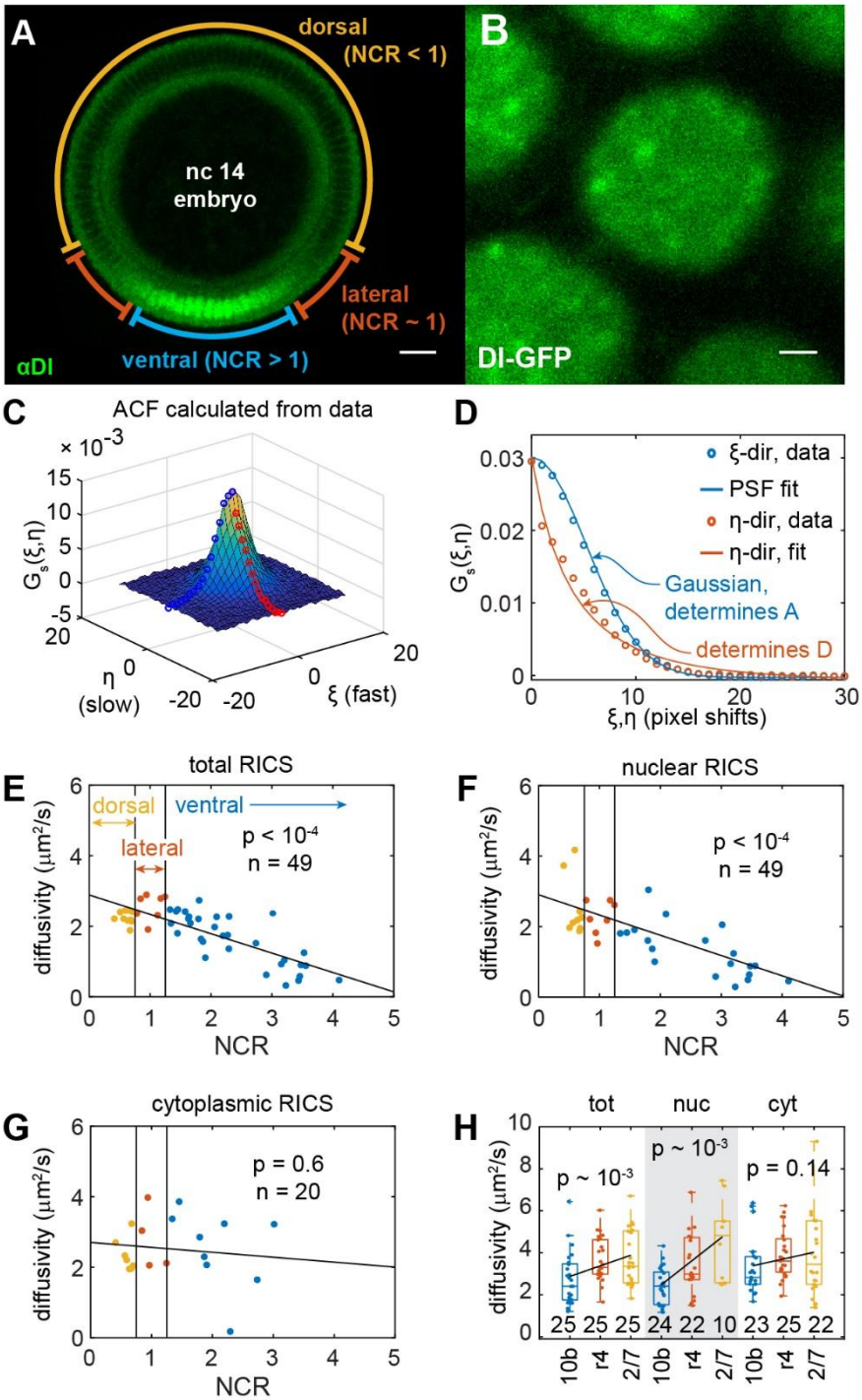

Figure 1: RICS analysis reveals a dorsal-ventral asymmetry in the mobility of Dl. (A) Representative image of the Dl gradient in an nc 14 embryo. Scale bar = 25 μm. (B) Representative image of Dl-GFP used for RICS analysis. Scale bar = 1 μm. (C,D) Plots of the autocorrelation function (ACF) of the image in A. (C) 3D plot of the ACF. Blue and red open circles represent the slice of the 3D surface for the fast and slow directions, respectively. (D) Plot of the fast and slow slices of the 3D ACF. Blue and red open circles (experimental data) correspond to those found in (C). The experimental data (open circles) are fit using a diffusion model (solid curves). The data

869 and fit are separated into two components, the “fast” (ξ, blue) and “slow” (η, orange) directions.
870 (E-G) Plots of the diffusivity of Dl-GFP vs NCR, measured using RICS on the entire imaging
871 frame (nuclear plus cytoplasmic) (E), nuclear regions only (F), or cytoplasmic regions only (G).
872 (H) Boxplot of the diffusivity of Dl-GFP in mutant embryos measured using RICS on the entire
873 imaging frame (nuclear plus cytoplasmic) (“tot”; left side), nuclear regions only (“nuc”; center,
874 gray), or cytoplasmic regions only (“cyt”; right side). In (E-H), blue represents ventral/“ventral-
875 like”, orange represents lateral/“lateral-like”, and yellow represents dorsal/“dorsal-like”
876 measurements. Solid dots represent individual measurements. Black lines represent a linear
877 regression fitted to the data. *p*-values for the slope of the trendline being zero are indicated on the
878 graph. Sample sizes indicated on graph.
879

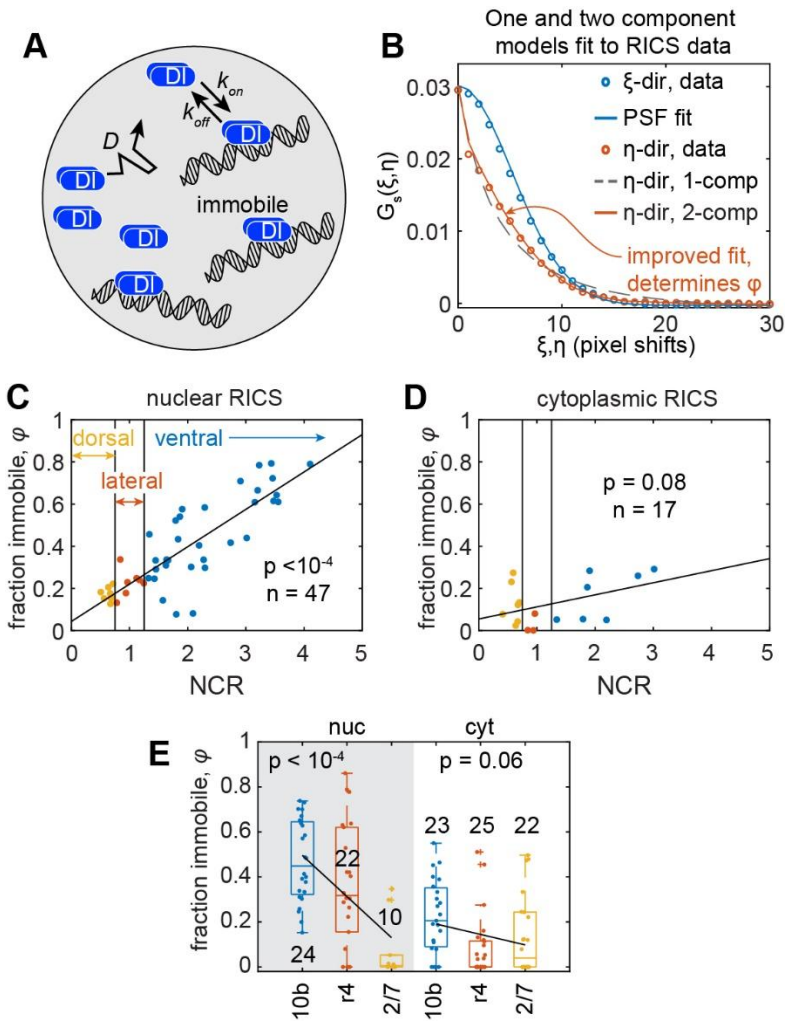

Figure 2: One- and two-component diffusion models quantify the relationship between DNA binding and mobility of Dl. (A) Illustration of the two-component model. Dl can diffuse and reversibly bind DNA. Dl bound to DNA is immobile. In contrast to the one-component diffusion model, in which Dl is freely diffusible and does not bind to DNA. (B) Comparison of one-component (dashed gray curve) and two-component (solid orange curve) diffusion models fit to the slow direction of the experimental RICS data (orange open circles). (C,D) Plots of the fraction of immobilized Dl (φ) vs. NCR measured using RICS on nuclear regions only (C) or cytoplasmic regions only (D). (E) Boxplot of φ in mutant embryos measured using RICS on nuclear regions only ("nuc"; left side, gray) or cytoplasmic regions only ("cyt"; right side). In (C-E), blue represents ventral/"ventral-like", orange represents lateral/"lateral-like", and yellow represents dorsal/"dorsal-like" measurements. Solid dots represent individual measurements. Black lines represent a linear regression fitted to the data. *p*-values for the slope of the trendline being zero are indicated on the graph. Sample sizes indicated on graph.

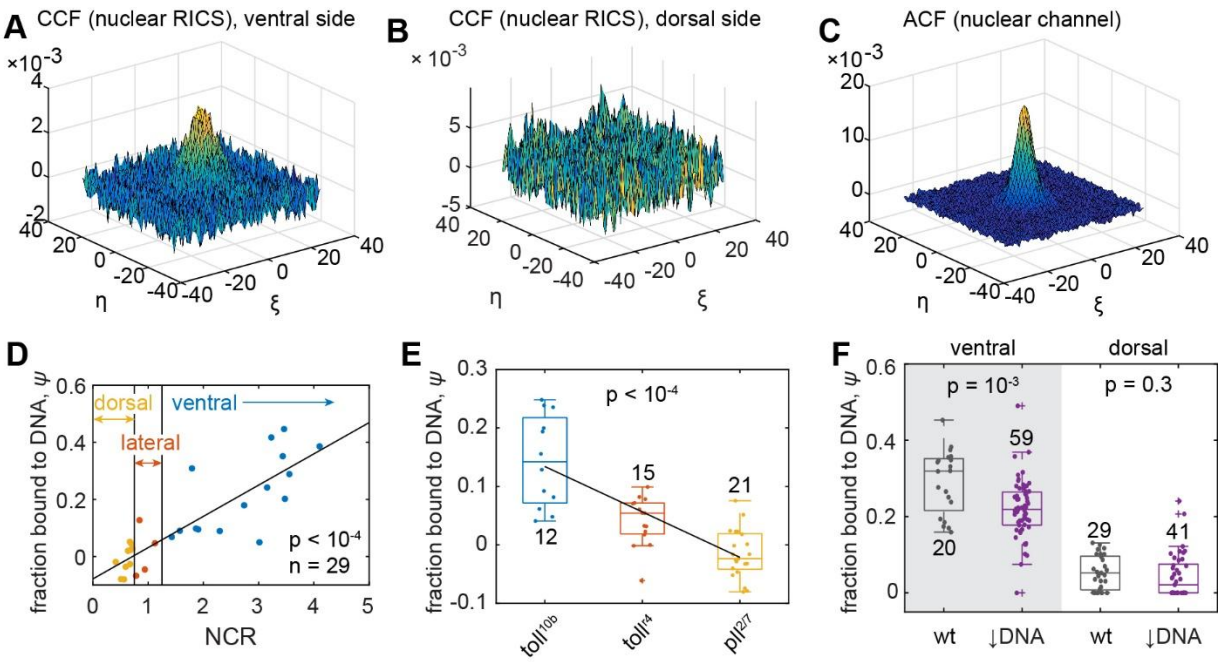

Figure 3: Cross-correlation RICS analysis of DNA-bound Dl. (A,B) Cross-correlation between Dl-GFP and H2Av-RFP, with nuclear mask, on the ventral side (A) or the dorsal side (B). (C) Example of autocorrelation function of H2Av-RFP, with nuclear mask. (D) Plot of ψ, the fraction of Dl bound to DNA, in wildtype embryos vs. NCR. (E) Boxplot of ψ in Toll signaling mutant embryos. In (D,E), blue represents ventral/"ventral-like", orange represents lateral/"lateral-like", and yellow represents dorsal/"dorsal-like" measurements. Solid dots represent individual measurements. Black lines represent a linear regression fitted to the data. *p*-values for the slope of the trendline being zero are indicated on the graph. (F) Boxplot of ψ, the fraction of Dl bound to DNA, in either wildtype (wt) embryos or embryos overexpressing a mutated form of Dl (R063C) with reduced DNA binding (↓DNA). Left side of plot (gray): ventral side; right side of plot (white): dorsal side. *p*-values for differences in means of the distributions are indicated on the graph. In (D-F): Sample sizes indicated on graph.

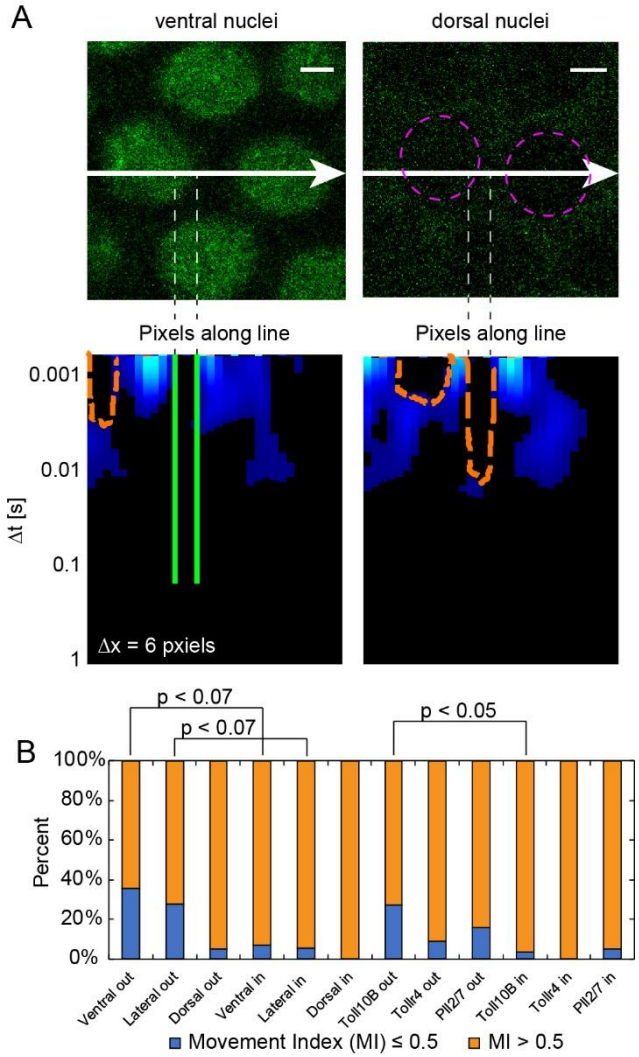

Figure 4: pCF analysis reveals a dorsal-to-ventral asymmetry in nuclear export of Dl. (A) Representative images of Dl-GFP on the ventral (top left image) and dorsal (top right image) sides of the embryo with their respective pCF carpets (bottom left and bottom right). Scale bar = 2um. White arrows represent the direction and y-coordinate of the pCF line scan. Magenta circles in dorsal side image outline the two nuclei crossed by the line scan. Dashed vertical lines illustrate two cases of locations in the images where a crossing of the nuclear envelope is observed (inside the nucleus to outside). A Dl-GFP molecule observed on the left vertical line (inside the nucleus) may or may not be detected at the location of the right vertical line (outside) at a later time point. Orange, dashed lines in the carpet label arches which indicate delayed Dl-GFP movement, while green, solid lines demarcate black regions of the carpet which indicate no Dl-GFP movement. (B) Percent of embryos that have high (Movement Index (MI) > 0.5, orange) and low (MI ≤ 0.5, blue) Dl-GFP movement either out of (out) or into (in) the nucleus. * denotes p<0.07, ** denotes p<0.05, Chi-squared test with likelihood ratio.

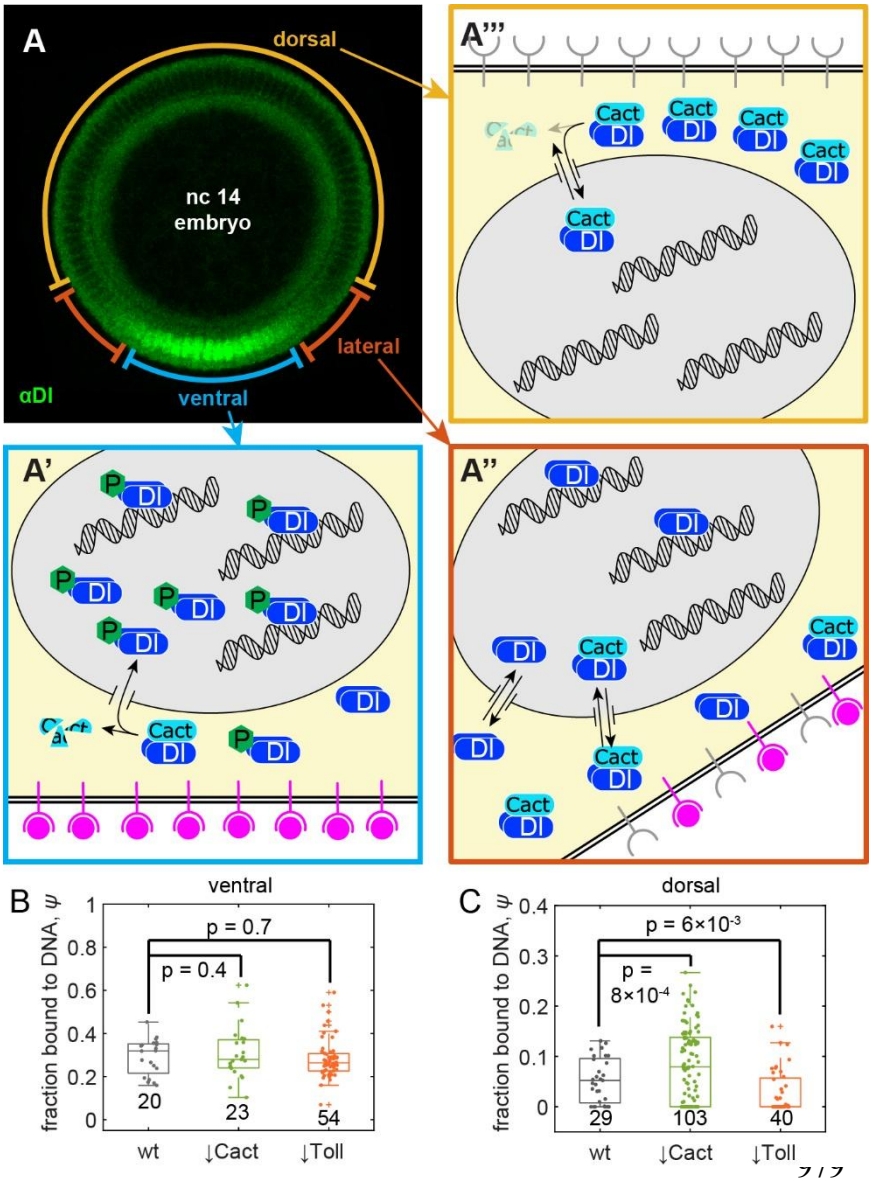

Figure 5: Variation of Dl mobility along the DV axis is due to presence of Cact in the nuclei. (A) (top left) Depiction of the different embryo domains, ventral (blue region), lateral (orange region), and dorsal (yellow region). Same embryo as in Fig. 1A. (A') Schematic of ventral side of embryo. High levels of activated Toll (magenta receptors) result in the destruction of Cact and phosphorylation of Dl. Free Dl enters the nucleus, so GFP fluorescence is mostly nuclear. Free Dl in the nucleus binds to DNA, which lowers the overall mobility of Dl species, and exits the nucleus at a slow rate. (A'') Schematic of lateral domain of embryo. Lower levels of Toll activation lead to a mixture of free and Cact-bound Dl. Nuclear and cytoplasmic levels of GFP fluorescence are roughly equal. Dl has a higher mobility due to lower fraction of Dl bound to the DNA. Dl exits the nucleus faster than on the ventral side. (A''') Schematic of the dorsal domain of the embryo. Little-to-no free Dl is present, so Dl-GFP fluorescence is mostly cytoplasmic. High mobilities stem from no DNA binding. (B,C) Boxplots of ψ, the fraction of Dl bound to DNA for the UAS-dl^{wt}-*gfp* (control), UAS-dl^{S234P}-*gfp* (reduced Cact binding: ↓Cact), and UAS-dl^{S317A}-*gfp* (reduced Toll phosphorylation: ↓Toll) alleles on the ventral (B) or dorsal (C) sides. The median line for S317A in (C) is located at ψ = 0. Solid dots represent individual measurements. *p*-values for pairwise comparisons to the control are indicated on the graph. Sample sizes indicated on graph.